energies

Article

Development and Experimental Implementation of Optimized PI-ANFIS Controller for Speed Control of a Brushless DC Motor in Fuel Cell Electric Vehicles

Abdessamad Intidam, Hassan El Fadil *, Halima Housny, Zakariae El Idrissi, Abdellah Lassioui, Soukaina Nady and Abdeslam Jabal Laafou

ISA Laboratory, ENSA, Ibn Tofail University, Kenitra 14000, Morocco; intidam.abdessamad@gmail.com (A.I.)
* Correspondence: elfadilhassan@yahoo.fr

Abstract: This paper compares the performance of different control techniques applied to a high-performance brushless DC (BLDC) motor. The first controller is a classical proportional integral (PI) controller. In contrast, the second one is based on adaptive neuro-fuzzy inference systems (proportional integral-adaptive neuro-fuzzy inference system (PI-ANFIS) and particle swarm optimization-proportional integral-adaptive neuro-fuzzy inference system (PSO-PI-ANFIS)). The control objective is to regulate the rotor speed to its desired reference value in the presence of load torque disturbance and parameter variations. The proposed controller uses a dSPACE platform (MicroLabBox controller board). The experimental prototype comprises a PEMFC system (the Nexa Ballard FC power generator: 1.2 kW, 52 A) and a brushless DC motor BLDC of 1 kW 1000 rpm. The PSO-PI-ANFIS controller presents better performance than the PI-ANFIS and classical PI controllers due to its ability to optimize the PI-ANFIS controller's parameters using the particle swarm optimization (PSO) algorithm. This optimization results in improved tracking accuracy and reduced overshoot and settling time.

Keywords: PEM fuel cell; brushless DC (BLDC) motor; proportional integral controller (PI); adaptive neuro-fuzzy inference system (ANFIS); particle swarm optimization (PSO); speed control; dSPACE DS1202 real-time control (RTC) card; experimental validation

check for updates

Citation: Intidam, A.; El Fadil, H.; Housny, H.; El Idrissi, Z.; Lassioui, A.; Nady, S.; Jabal Laafou, A. Development and Experimental Implementation of Optimized PI-ANFIS Controller for Speed Control of a Brushless DC Motor in Fuel Cell Electric Vehicles. *Energies* **2023**, *16*, 4395. https://doi.org/10.3390/en16114395

Academic Editors: Alberto Reatti and Tek Tjing Lie

Received: 3 April 2023
Revised: 12 May 2023
Accepted: 23 May 2023
Published: 29 May 2023

1. Introduction

In view of the recent disturbances in the air due to pollution, as well as the depletion of and the costs of extracting fossil fuels, which are increasing with time [1], scientific research is accelerating to find alternatives to replace fossil fuels with the aim to cease using them altogether; among these alternatives, for example, fuel cells [2–4] have recently begun to be considered along with batteries and supercapacitors, and many car companies have started to design, develop, and implement fuel cell systems into the motors of electric cars [5,6]. For fuel cells, we find brushless DC motors that combine the features of both DC motors as well as induction motors. It is expected that, by 2030, BLDC motors will become the dominant power transmission method in various industries, replacing traditional induction motors [7].

Developing independent energy sources, especially clean and economically viable sources, is one of the significant technological challenges currently being faced. The use of an electric motor, with high energy efficiency and silent and non-polluting operation, seems to be the ideal solution, and many studies have been carried out to study the effect of the load change on a brushless DC motor [8–10], while limited studies have investigated the speed regulation of a motor powered by a fuel cell [11–13].

To drive a light motorcycle, Kim et al. (2009) built an experimental prototype of a fuel cell-powered motor/generator and controlled the motor via a classic PI controller, but the results they obtained showed that the motor speed exceeded the reference speed [13]. While Tsotoulidis et al. (2013) proposed controllers called MRPID, which is a method that improves control dynamics and system stability, and compared it with a classic PI controller, but after looking at the results, which show the superiority of the latter [14]. Feyzi et al. (2011) controlled the speed by regulating a parameter of the PID unit by exploiting an algorithm called particle swarm optimisation (PSO) to achieve a better dynamic response [15]. Then comes Yigit et al. (2020) by building the system comprising a fuel cell, electrolyzer, and brushless DC motor on MATLAB software and using a closed-loop FOPI controller whose parameters are optimised by an algorithm called Moth Swarm (MSA). However, the results show that the motor speed exceeds the reference speed on the one hand, and on the other hand the fluctuations in the speed reached about 17 revolutions per minute [11].

Recently, with the complexity of systems and their non-linear nature, in addition to the difficulty of finding parameter values for the PI controller, and thanks to the development of microcontrollers and the increase in their computational speeds, researchers began to rely on algorithms as tuning techniques for adjusting the parameters of the controllers, easy to use and easy to program, and many of them applied these algorithms to regulate the speed of motors, including brushless DC motors used in many applications, including electric vehicles, in general, the optimization can be summarized as the best solution in terms of motor response time, fluctuations in speed, energy consumed by the motor, and effort applied to the fuel cell [16–18].

To date, very few studies have been able to implement a combination of classical PI controllers, Adaptive Fuzzy Inference System (ANFIS), and Particle Swarm Optimization (PSO), which is one of the most famous optimization algorithms applied in various fields, in order to improve the dynamic response of the motor, as well as maintain the life of the fuel cell, by reducing the peak current that the cell is subjected to when a sudden change in load occurs. Younus et al. (2023) performed a hybrid optimization of a gray wolf and a proportionally integrated controller. They compared it with a PID controller, a PSO-PI controller and an ANFIS controller to control the speed of a brushless DC motor. For the load and speed conditions of two variables, one fixed and the other variable, the simulation results showed that the controllers based on Hybrid GWO-PI are reliable compared to the control units under study [19]. However, these studies remain just simulations far from real systems, so we decided to test these controllers on a real platform, then design and build them inside the laboratory to remove confusion and confirm or deny the results obtained in the literature that was then listed. Among these controllers tested on the mentioned platform, we cite the PI controller, the PI-ANFIS controller, and the PSO-PI-ANFIS controller. The experimental results showed the superiority of controllers with optimization algorithms, including the PSO-PI-ANFIS controller.

The Purpose of This Article

The purpose of this research is to present the principles of the initial design of a BLDC control system that works on fuel cell energy and as an environmentally friendly source that has recently begun to be used in electric vehicles by relying on components, then designing and manufacturing them in the laboratory, and others and then purchasing them, to conduct laboratory tests of advanced algorithms. On a real platform that gives readers a clear idea, as well as an idea of the design, it can be created in any country to try all kinds of algorithms, including advanced and classic ones. Design, simulation, and experimental study of a 1 kW brushless DC motor used in electric vehicles have been achieved.

2. System Overview

Tested on a small scale in the laboratory, the new topology of an electric vehicle powered by a clean energy source, which is the fuel cell (FC), is illustrated in Figure 1. This energy source converts hydrogen supplied through tanks into electric current by chemical reactions between hydrogen and air. It needs two DC/DC converters connected to a standard DC traction bus. It is, therefore, through them that the fuel cell's power will pass to the traction motor, which is a brushless direct current motor (BLDC) driven by a DC-to-AC converter. In addition, the system consists of an auxiliary services unit, sensors for measuring voltage, current, torque, and speed, and three hall effect sensors used to detect the position of the rotor, and, finally, the MicroLabBox controller board (dSPACE DS 1202 platform). These devices have been selected from commercially available components. The FC is the primary energy source of the electric vehicle. It is connected to a buck-boost-type unidirectional DC/DC converter that stabilizes the unregulated fuel cell voltage of the Nexa® 1200 fuel cell module to 24 Volt direct current. It also protects the system against reverse currents. In addition, the DC/DC converter is connected to a boost-type bidirectional DC/DC converter which raises the low DC voltage delivered by the FC converter, which is 24 V, to the traction standard DC bus, which is 48 V. The three-phase BLDC motor is easy to spin. The control is based on the conversion of direct current into alternating current. For this, a three-phase inverter is required. The inverter comprises power switches, such as MOSFETs or IGBTs, chosen according to the required power and efficiency. The DC to AC inverter is selected to fit with the motor used to switch. This driver is controlled according to the signals from the Hall effect sensors and using the Pulse Width Modulation (PWM) control strategy. Motor voltage, current, and speed are controlled by changing the duty cycle (D) of the PWM signal. Hall effect sensors are placed on the stator, and their signals vary from a high state to a low state during the rotation of the motor (the low/high state is output when a North/South magnetic pole is detected).

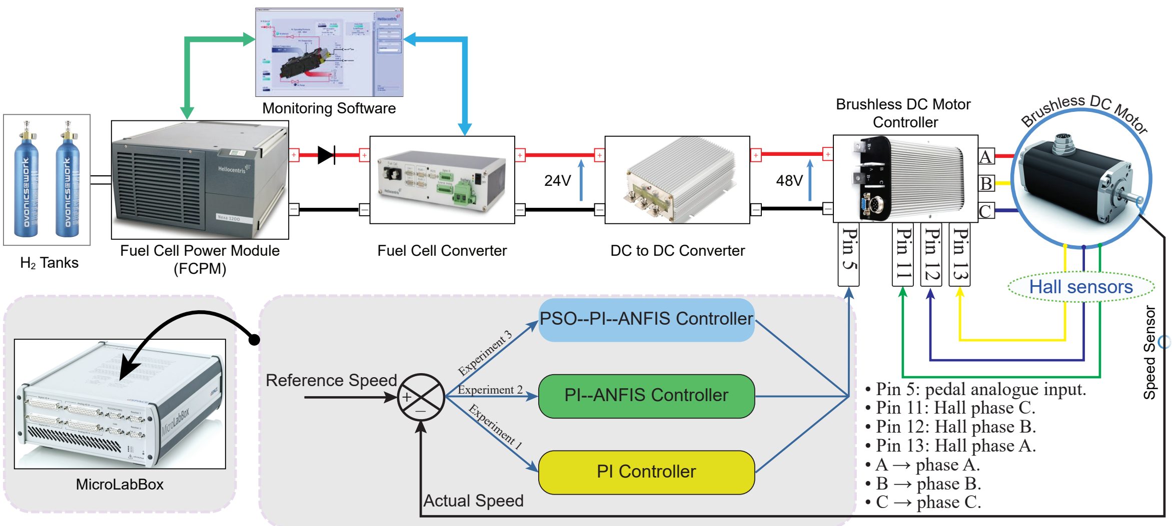

Figure 1. Schematic diagram of the BLDC control system in an FCEV application.

3. System Modelling

3.1. Fuel Cell Modeling

Due to factors such as the low operating temperature, high-power density, efficiency, and relative ability to quickly adapt to traction motor demands in terms of changes in power, PEM FC can be considered a suitable option for public transport applications. A Nexa® 1200, a fully integrated fuel cell power module based on the FCgen™ 1020 ACS stack from Ballard's, has been selected in this work, which presents a rated power of 1.2 kW–24 V.

In this work, we consider the static (current-voltage) characteristic of the PEMFC, as shown in Figure 2. This non-linear characteristic [20] depends on the thermodynamically predicted fuel cell voltage output and three major losses, activation losses (due to electrochemical reaction), ohmic losses (due to ionic electronic condition), and concentration losses (due to mass transport). A reduced model represents the behavior of this FC to consider the FC dynamics. This equivalent electric circuit, illustrated in Figure 3, is used [21,22].

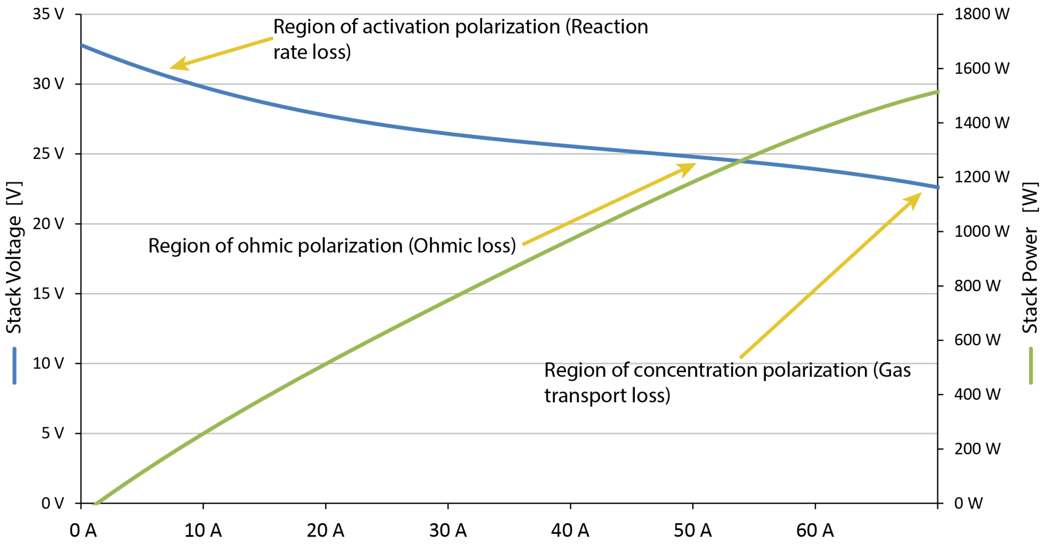

Figure 2. Fuel cell V–I characteristics and output power curve.

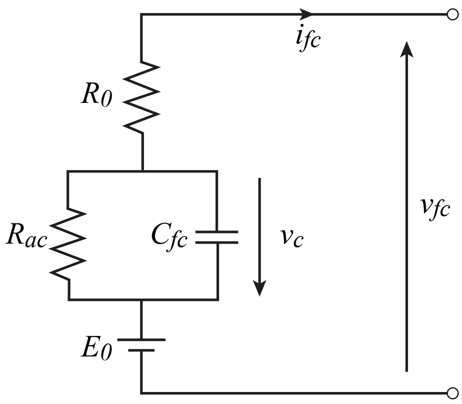

Figure 3. Equivalent electric RC circuit of a fuel cell stack.

Then, the FC voltage is governed by the following equations,

$$v_{fc} = E_0 - R_0 i_{fc} - v_c \quad (1)$$

$$\frac{dv_c}{dt} = -\frac{1}{\tau_{fc}} v_c + \frac{1}{C_{fc}} i_{fc} \quad (2)$$

where E_0 is the open circuit voltage, R_0 is the ohmic resistance, C_{fc} is the equivalent electrical capacitance, $\tau_{fc} = C_{fc} R_{ac}$ is the fuel cell electrical time constant, and R_{ac} represents the equivalent series resistance of the activation and concentration resistances [23].

3.2. Mathematical Model of the BLDC (Brush Less Direct Current Motor)

Regarding the BLDC motor, different analytical models could be considered. In this work, BLDC motor modelling is based on phase variables (abc) as an easy-to-design tool for developing BLDC motor controls. Three phase BLDC motor is usually modelled as a series connection of stator winding resistance, inductance and back–emf as shown in Figure 4.

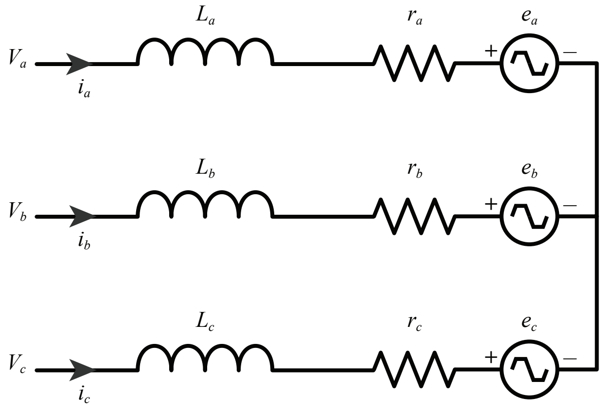

Figure 4. Equivalent circuit of the BLDC motor.

For simplification purposes, the model will be based on the following assumptions. The air gap is uniform; the magnetic circuit is unsaturated and does not take into account losses by eddy currents or by hysteresis; the three phases of the stator are symmetrical and identical. Therefore, Equation (3) presents the BLDC motor voltages.

$$\begin{bmatrix} V_a \\ V_b \\ V_c \end{bmatrix} = \begin{bmatrix} r_a & 0 & 0 \\ 0 & r_b & 0 \\ 0 & 0 & r_c \end{bmatrix} \begin{bmatrix} i_a \\ i_b \\ i_c \end{bmatrix} + \frac{d}{dt} \begin{bmatrix} L_a & M_{ab} & M_{ac} \\ M_{ba} & L_b & M_{bc} \\ M_{ca} & M_{cb} & L_c \end{bmatrix} \begin{bmatrix} i_a \\ i_b \\ i_c \end{bmatrix} + \begin{bmatrix} e_a \\ e_b \\ e_c \end{bmatrix} \quad (3)$$

where V_a, V_b and V_c are phase voltages; r_a, r_b, and r_c are stator winding resistances; L_a, L_b, and L_c are the self-inductances of the stator winding; M_{ab}, M_{ac}, and M_{cb} are mutual inductances; i_a, i_b, and i_c are the phase currents; and e_a, e_b, and e_c are the back emf forces.

From the assumptions mentioned above, it can be deduced that $L_a = L_b = L_c = L$, $r_a = r_b = r_c = r$, and $M_{ab} = M_{ac} = M_{cb} = M$.

In addition, the three-phase winding is connected in a star, which makes it possible to mention the following simplification:

$$i_a + i_b + i_c = 0 \Longrightarrow i_b + i_c = -i_a \quad (4)$$

Equation (3) is thus derived as follows:

$$Li_a + Mi_b + Mi_c = Li_a + M(-i_a) = (L - M)i_a \quad (5)$$

Therefore, after repeating the same calculation steps for the other two phases, Equation (3) becomes

$$\begin{bmatrix} V_a \\ V_b \\ V_c \end{bmatrix} = \begin{bmatrix} r & 0 & 0 \\ 0 & r & 0 \\ 0 & 0 & r \end{bmatrix} \begin{bmatrix} i_a \\ i_b \\ i_c \end{bmatrix} + \frac{d}{dt} \begin{bmatrix} L_s & 0 & 0 \\ 0 & L_s & 0 \\ 0 & 0 & L_s \end{bmatrix} \begin{bmatrix} i_a \\ i_b \\ i_c \end{bmatrix} + \begin{bmatrix} e_a \\ e_b \\ e_c \end{bmatrix} \quad (6)$$

where $L_s = L - M$ is the equivalent phase inductance.

Regarding the speed of the motor, it is necessary first to present the mechanical equations of the motor. The electromagnetic torque and the speed derivative are expressed as follows,

$$T_e = T_L + J\frac{d\Omega}{dt} + B\Omega \quad (7)$$

$$T_e = \frac{i_a e_a + i_b e_b + i_c e_c}{\Omega} \quad (8)$$

where Ω is the mechanical speed of the motor (rad/s), J is the moment of inertia, B is the coefficient of friction, and T_L is the resistive torque.

4. Drive Operation and BLDC Motor Controller Description

4.1. Drive Operation

When using the full-bridge inverter for BLDC motor control, two phases of the three-phase winding system are supplied from the input voltage to maintain the angle between the flux of the stator and the rotor at nearly 90°. For this purpose, switching is triggered after every 60° electrical degree. Figure 5. illustrates a schematic of a three-phase full-bridge inverter, and Figure 6 describes the waveform of the phase currents and those of the trapezoidal emf forces as well as the variations of the signals of the Hall effect sensors as a function of the electrical degree (each electrical degree of 60° is considered as an interval).

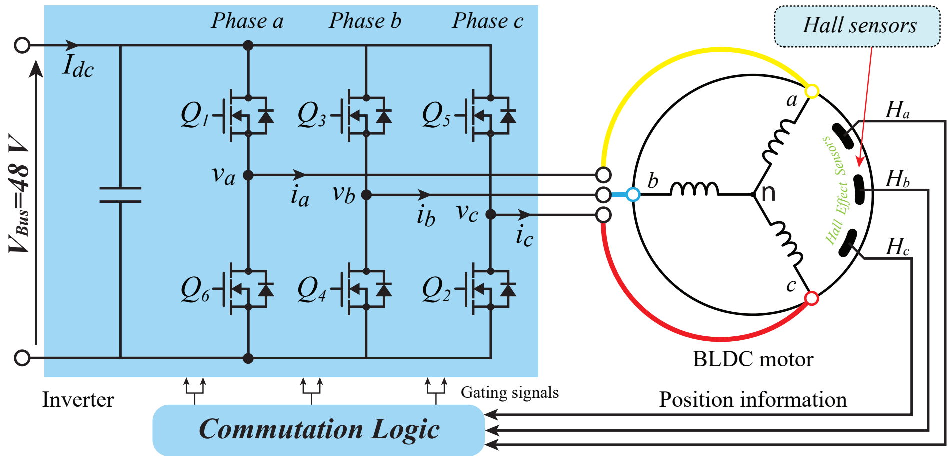

Figure 5. Full bridge three-phase BLDC motor control scheme.

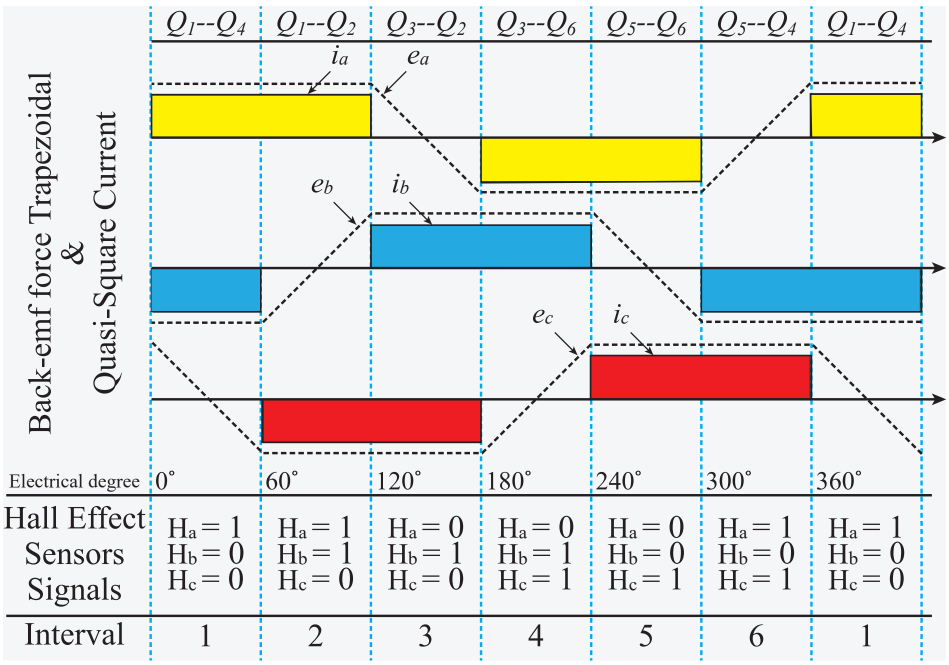

Figure 6. Ideal back –emfs, phase currents, and position sensor signal as a function of electrical degree.

Figure 6 depicts the Hall effect sensor signals (Ha, Hb, Hc) in relation to the back-electromotive forces (back-emfs) (e_a, e_b, e_c) of the stator windings, as shown in Figure 5. These sensor signals are closely related to the phase currents (i_a, i_b, i_c) in the motor. The states of the MOSFETs $(Q_1, Q_2, Q_3, Q_4, Q_5, Q_6)$ change after every 60° electrical degree, coinciding with a change of state of a Hall effect sensor (Ha, Hb, Hc) . These sensors are placed on the stator with a well-defined position and a distance of $\frac{2\pi}{3p}$ between every two successive sensors (p is the number of pole pairs). Table 1 presents the state of the MOSFETs of the inverter, the signals of the Hall effect sensors and the sign of the current on each phase of the stator to turn the motor.

Table 1. Combination of Hall sensors and phase signals.

Switching Interval (°)	Seq. Number	Pos. Sensors			Switch Closed		Phase Current		
		Ha	Hb	Hc			A	B	C
0°–60°	1	1	0	0	Q_1	Q_4	$+I_{dc}$	$-I_{dc}$	off
60°–120°	2	1	1	0	Q_1	Q_2	$+I_{dc}$	off	$-I_{dc}$
120°–180°	3	0	1	0	Q_3	Q_2	off	$+I_{dc}$	$-I_{dc}$
180°–240°	4	0	1	1	Q_3	Q_6	$-I_{dc}$	$+I_{dc}$	off
240°–300°	5	0	0	1	Q_5	Q_6	$-I_{dc}$	off	$+I_{dc}$
300°–360°	6	1	0	1	Q_5	Q_4	off	$-I_{dc}$	$+I_{dc}$

4.2. BLDC Motor Controller Description

Five metal strips and an aviation plug (J2) provide a grounding environment for the battery, motor, and controller signals. As shown in Figure 7.

- B+: battery positive.
- B−: battery negative pole.
- A: Output U/1/A phase, connected to the thick red wire of the motor.
- B: Output V/2/B phase, connected to the thick yellow wire of the motor.
- C: Output W/3/C phase, connected to the thick blue wire of the motor.

J2 pin definition:

- Pin 1: PWR: Control power supply.
- Pin 2: GND: signal ground or power ground.
- Pin 3: GND: Signal ground.
- Pin 4: 12 V high-level brake and motor temperature sensor signal input.
- Pin 5: pedal analogue input, 0–5 V.
- Pin 6: Brake analogue input, 0–5 V.
- Pin 7: 5 V: 5 V power output, 40 mA
- Pin 8: pedal safety switch input.
- Pin 9: Reversing switch input.
- Pin 10: Brake switch input.
- Pin 11: Hall phase C, connected to the motor's thin green Hall signal wire.
- Pin 12: Hall phase B, connected to the motor's thin blue Hall signal wire.
- Pin 13: Hall phase A, connected to the motor's thin yellow Hall signal wire.
- Pin 14: GND, signal ground.

Notes:

- All GND pins (pin 2, pin 3, pin 14) are internally connected. GND is internally connected to B−.

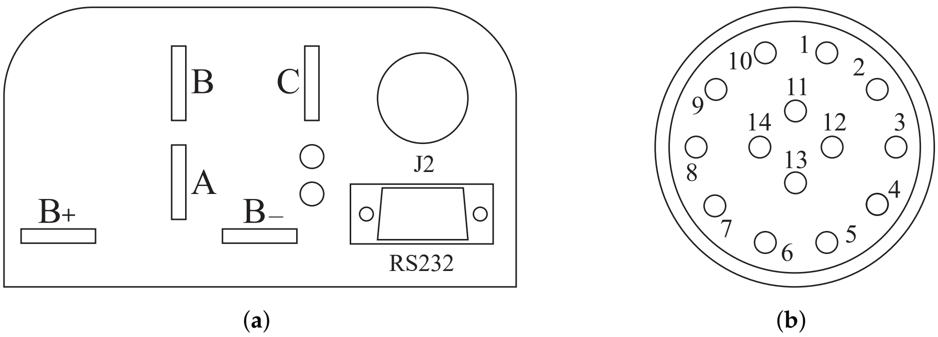

Figure 7. brushless DC motor controller: (**a**) metal strips. (**b**) J2 pin.

5. Control Design for BLDC Motor

Recently, researchers have been using fuzzy logic in hybrid control to improve the efficiency of conventional controllers and enhance the performance characteristics of the control. Indeed, the most common hybrid control, including fuzzy logic control, is the fuzzy PID control strategy. In this intelligent hybrid technique, the fuzzy controller is often used to adjust the PID controller parameters. Combining fuzzy logic control technology with traditional PID controllers is intended to achieve enhanced controller behavior and a better control system [24].

However, the design of the fuzzy controller is considered a complicated task despite the wide use of the fuzzy logic system in control engineering. Indeed, to define the fuzzy rules of the fuzzy controller, we need a minimum knowledge of the system's functioning. This implies that we should determine the membership function type and degree. Therefore, the most common hybrid architecture that combines the fuzzy logic and the neural network, the Adaptive Neuro-Fuzzy Inference System (ANFIS), was proposed to adjust the gains of the PI controller online to stabilize the electric vehicle system in speed control [25].

5.1. Adaptive Neuro-Fuzzy Inference System Architecture

Jang first proposed Adaptive Neuro-Fuzzy Inference Systems (ANFIS) in 1993 [26]. The learning process by neural networks automatically adapts the membership functions (MF) and the fuzzy inference system (FIS) parameters using the training input–output dataset. For simplicity, two inputs and a single output are used in the ANFIS architecture. Figure 8 shows the ANFIS architecture for a Sugeno–Fuzzy model with nine rules. In particular, it is shown that the unique output y_s (corresponding to the PI controller gains) is calculated directly by weighting the two inputs x_1 and x_2 (corresponding to error signal e and $\int e\,dt$ its integral action) according to the fuzzy rules of three membership functions ($A^1_{1,2,3}$ and $A^2_{1,2,3}$) through five layers. Each layer in the ANFIS architecture contributes to the learning process of the FIS. The ANFIS structure is described layer by layer below [27,28].

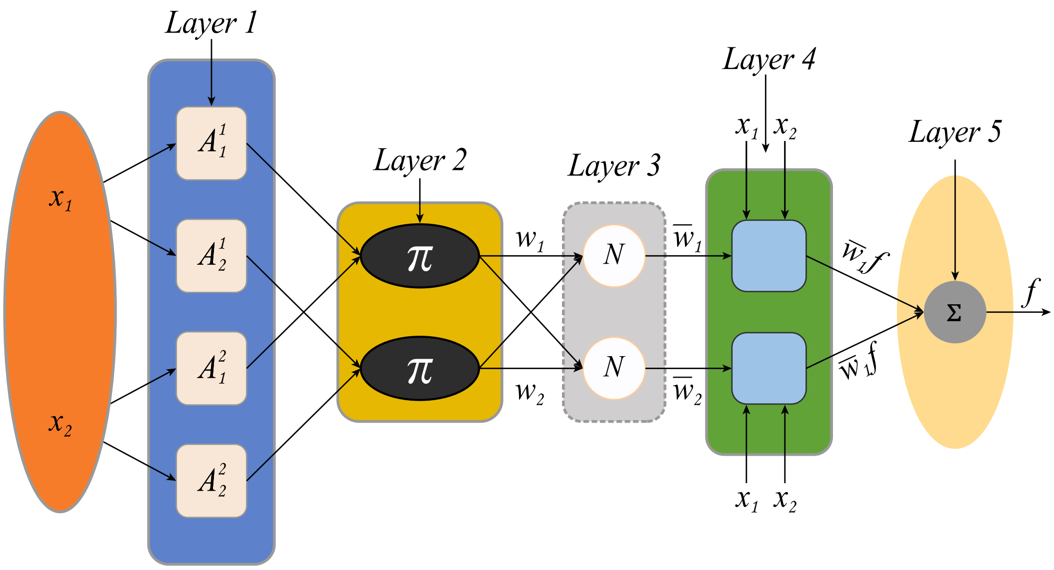

Figure 8. The architecture of the ANFIS model.

Layer 1 (Fuzzification layer): Each node corresponds to a function parameter. The output from each node is determined by the membership function degree of each input x_1 and x_2 as follows,

$$\begin{cases} O^1_{i,1} = \mu_{A^1_i}(x_1) \\ O^1_{i,2} = \mu_{A^2_i}(x_2) \end{cases} \tag{9}$$

where i corresponds to the membership function number ($i = 1, 2, 3$) and A_i^1 and A_i^2 are the linguistic label associated with the node function i.

Layer 2 (Rule layer): Each node in this layer is a fixed node, and the circular node is labelled as π. The output node is the product result of the incoming node signals. A current node receives inputs from the respective nodes of the layer to generate a firing strength for each rule as follows,

$$O_k^2 = w_k = \mu_{A_i^1}(x_1)\mu_{A_i^2}(x_2) \tag{10}$$

where $k = \{1, \ldots, 9\}$ denotes the Sugeno–Fuzzy rules and the output w_k is the firing strength of each rule.

Layer 3 (Normalization layer): Each node in this layer is a fixed node, and the circular node is labelled as N. Thus, in this layer, each node receives inputs from all the second layer nodes to compute the normalized firing strength of a given rule: the $i-th$ rule firing strength is divided by the sum of the firing of all rules to determine the value of each node.

$$O_k^3 = \overline{w}_k = \frac{w_k}{\sum_{j=1}^{9} w_j} \tag{11}$$

Layer 4 (Defuzzification layer): The fourth layer includes an adaptive node that produces a weighted output of each rule. Thus, each node is directly attached to the corresponding normalization node with initial inputs (x_1, x_2) to give a weighted value of each rule, defined by

$$O_k^4 = \overline{w}_k f_k = \overline{w}_k(p_k x_1 + q_k x_2 + r_k) \tag{12}$$

where $\overline{w}_k$ is the normalized firing strength provided by the third layer and the node parameters $\{p_k, q_k, r_k\}$ are also denoted as consequent parameters.

Layer 5 (Output layer): The unique node is a fixed node, and the circular node is labelled as $\sum$. This node is the result of the sum of all incoming inputs and provides an overall output defined by:

$$O_1^5 = \sum_{k=1}^{9} \overline{w}_k f_k \tag{13}$$

5.2. PI-ANFIS Controller for BLDC Motor

In this work, the control of the Brushless DC motor is based on a PI-ANFIS controller, which was developed by combining the conventional PI control strategy with the ANFIS controller. Figure 9 and Table 2 show the structure of the PI-ANFIS controllers, which is applied to the system's transfer function.

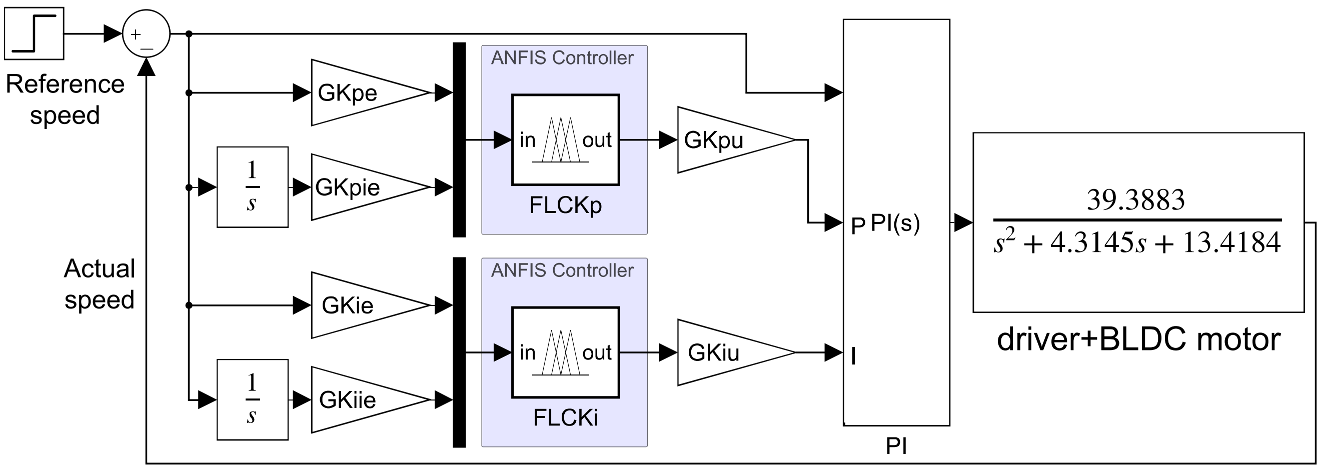

Figure 9. Structure of closed-loop ANFIS Controller.

Table 2. Parameters for the PI-ANFIS.

GK_{pe}	GK_{pie}	GK_{ie}	GK_{iie}	GK_{pu}	GK_{iu}
1	1	1	1	1	1

In this work, two PI-ANFIS controllers $ANFISK_p$ and $ANFISK_i$, are used for the k_p and k_i gains of the PI controller, respectively. For clarity, Algorithm 1 gives the main steps of the controller design process. Then a description of this algorithm is given below.

Algorithm 1 Main steps of the PI-ANFIS controller design

Begin
Collect initial dataset
Select training dataset
Set ANFIS parameters
Generate the two PI-ANFIS controllers
End

Step 1: The first step in the ANFIS controller design is collecting the training datasets. In this work, we use the PI control strategy [29], to collect the required dataset to design the two PI-ANFIS controllers for the BLDC motor system.

Then, to receive the necessary training data for the PI-ANFIS controllers, the response from the PI controller is collected. Significantly, the training dataset also consists of two-dimensional input vectors (the error e and $\int e\,dt$ its integral action) and a one-dimensional output vector y, the k_p or k_i PI controller gains.

Roughly two steps are involved in designing the ANFIS controller, the training and the testing process. In addition, the initial training data are arbitrarily separated into training data V_{train} (70% of the initial data) and the testing data V_{test} (30% of the initial data).

Step 2: The Fuzzy Inference System (FIS) approximation from the initial dataset requires defining the type and degree of the input-output membership functions (MFs). This work selects Gaussian input MFs for $ANFISK_p$ and $ANFISK_i$. In addition, it is assumed that linear output MFs generate the FIS structure of the two PI-ANFIS controllers. However, it is noteworthy that the degree of the membership functions significantly affects the computing time required for the controller design. A small MFs degree is particularly advantageous for the controller's computing time. In the proposed PI-ANFIS controllers, only three input MFs, are configured to implement each fuzzy inference system (FIS) of the controller. Table 3 also summarizes the other inference parameters.

Table 3. Inference system parameters.

Fuzzy Type	Defuzzification Method	Inference Engine
Takagi-Sugeno	*weighted average (wtaver)*	*prod-max*

Step 3: We generate the two PI-ANFIS controllers using many parameters, such as a vector of the training dataset V_{train}, the number of training epoch n_{epoch}, the training error E_{train}, and the optimization method. In practice, we have used the PI-ANFIS parameters given in Table 4.

Table 4. PI-ANFIS algorithm parameters.

Training Epoch Number n_{epoch}	Training Error Goal E_{train}	Optimization Method
20	0	Last-squares and back-propagation gradient descent

At the end of this step, two ANFIS controllers are generated.

5.3. PI-ANFIS Scaling Gains Tuning

To improve the performance characteristics of the resulting control system, we use the particle swarm optimization algorithm (PSO), as shown in Figure 10, to tune the PI-ANFIS controllers scaling gains [27,30]. The three scaling gains (GK_{pe},GK_{pie} and GK_{pu}) for the $ANFISK_p$ controller and (GK_{ie}, GK_{iie} and GK_{iu}) for $ANFISK_i$ controller should be fine-tuned.

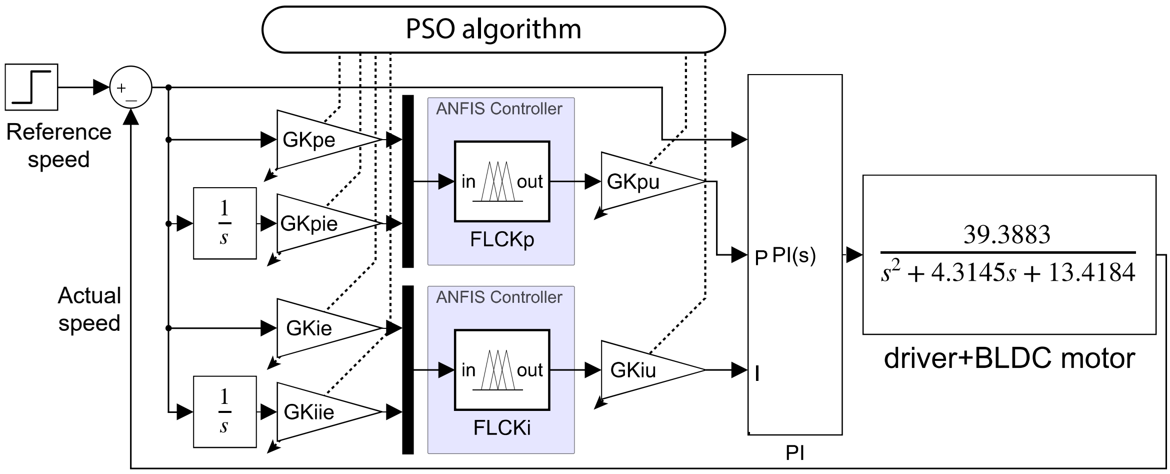

Figure 10. Tuning of ANFIS scaling gains with PSO algorithm.

Then, we start the optimization process by selecting the PSO parameters, such as population number (n), tune dimension (m), the maximum number of iterations (N_{iter}), and search space SS. The PSO parameters for tuning the PI-ANFIS scaling gains are summarized in Table 5.

Table 5. PSO parameters for the PI-ANFIS scaling gain tuning.

Gains	n	m	N_{iter}	S
$GK_{pe}, GK_{pie}, GK_{ie}, GK_{iie}$	200	3	5	$[0.01, 1.5]$
GK_{pu}	500	3	5	$[0.5, 1]$
GK_{iu}	500	3	5	$[0.1, 1]$

In this work, we use the well-known $ITAE$ objective function criterion defined in Equation (14) to evaluate the tuning of the PI-ANFIS scaling gains. After reaching the optimization process, the PSO algorithm delivers the appropriate six scaling gains, representing an essential element for designing an optimal PI-ANFIS controllers.

$$ITAE = \int_0^{\infty} t|e(t)|\, dt \tag{14}$$

6. Experimental Results and Discussion

6.1. Experimental Bench Description

Indeed, this experimental device makes it possible to develop and implement the various control algorithms, of course the speed or position control techniques of a brushless DC motor, as shown in Figure 11, the structure's overall electric motor drive is made up of several parts. Each of the details will be described below and with their electrical specifications.

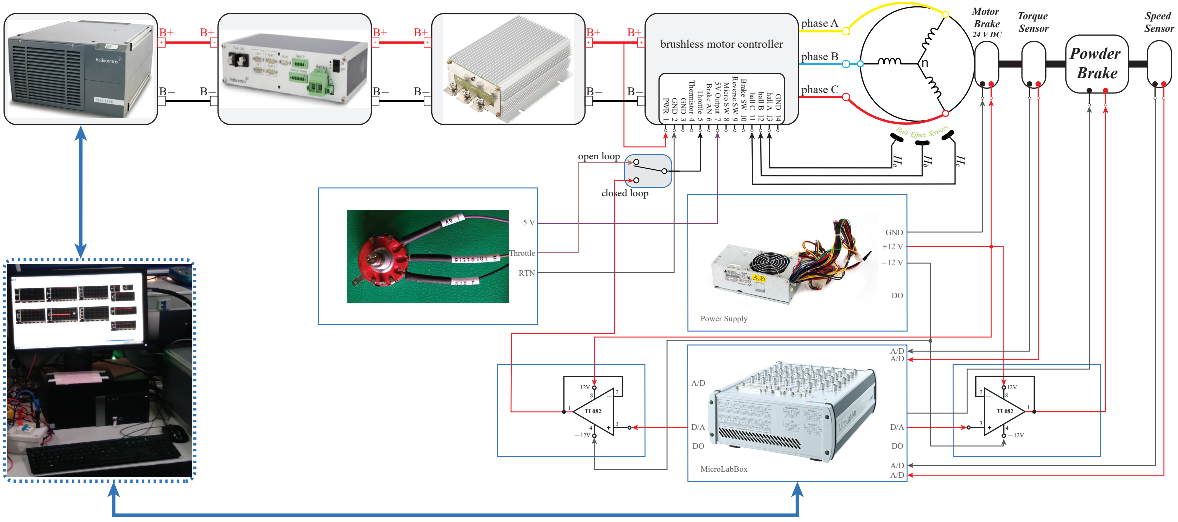

Figure 11. Diagram of the experimental device of the test bench.

dSpace board-based devices allow designers of electrical machinery control systems to significantly reduce development costs and time and increase control quality and performance. Figure 12 presents the entire test bench based on dSpace DS1202 implemented to develop an experimental device within our ISA laboratory at ENSA University Ibn Tofail dedicated to the control with the mechanical sensor of the BLDC.

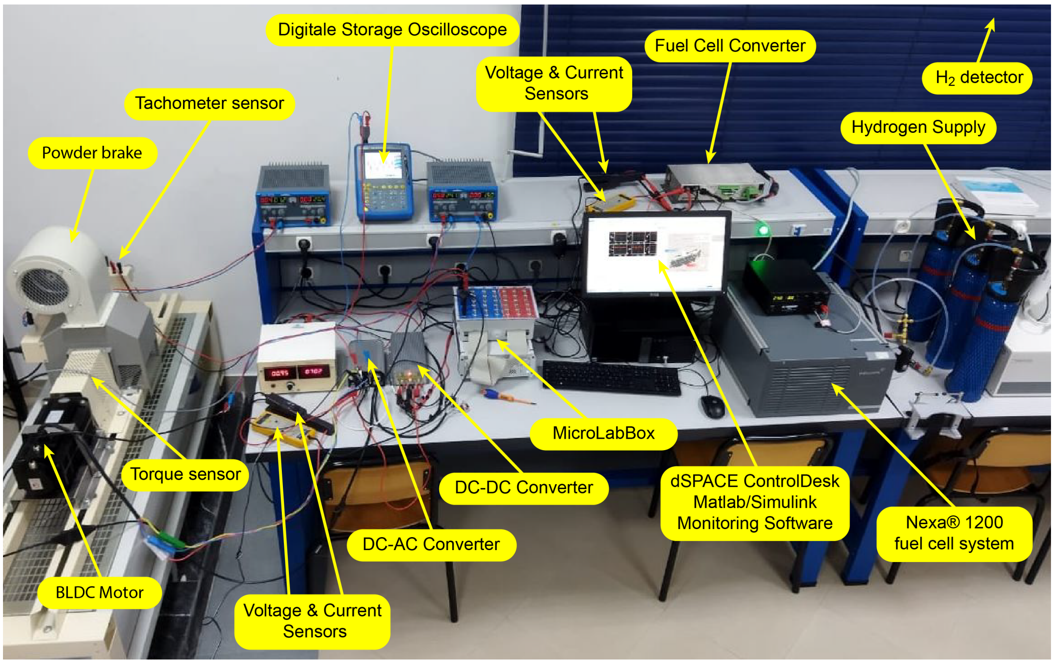

Figure 12. Laboratory prototype used for experimental validation.

In general, the entire test bench is composed of four groups, which are:

1. The energy source is the fuel cell of the PEM (proton exchange membrane) type. The Nexa® 1200 is a fully integrated fuel cell power module based on the FCgen™ 1020 ACS stack and DC/DC converter stabilizing the unregulated fuel cell voltage of the Nexa® 1200 fuel cell module to 24 Volt direct current from Ballard, its electrical data are presented, showing Table 6 and Table 7, respectively.

Table 6. Parameters of the Fuel Cell Power Module.

Parameter	Value
Rated power	1200 W
Rated current	52 A
Rated voltage	24 V
Output voltage (unregulated)	20. . . 36 V
Operational temperature	5. . . 40 °C

Table 7. Parameters of Fuel DC/DC Converter.

Parameter	Value
Output power	1200 W
Output current	max. 55 A
Nominal voltage	24 V
Output voltage	0. . . 32 V
Input voltage	16. . . 45 V
Operational temperature	−10. . . 55 °C
Efficiency	>96%

2. The DC brushless motor coupled to the powder brake presented in the power part of Figure 12 can provide an electromagnetic torque on the shaft of a maximum value equal to 10 Nm and a nominal mechanical power of 1.0 KW. The stator phases are star-coupled from Jiangsu Wheatstone Electrical Technology Co., Ltd. (Xueyan Town, Wujin, China). Motor specifications are shown in Table 8. The mechanical load comprises a powder brake fixed to the BLDC by a rigid coupling. The latter is intended to generate a resistive torque in both directions of machine rotation. It is controlled by the Metrix AX 502 Module, which we have configured in external mode.

Table 8. Parameters of the brushless DC motor.

Parameter	Value
Rated power	1000 W
Rated current	25.7 A
Rated voltage	48 V
Rated speed	1000 r/min
Rated torque	10 Nm

3. The DC–AC converter consists of a three-phase voltage inverter from Jiangsu Wheatstone Electromechanical Technology Co., Ltd. (Xueyan Town, Wujin, China) It is used to power the motor stator phases. Its characteristics are presented in Table 9. The adaptation of the control signal provided by the dSpace DS1202 card to the control input (pin 5) of the power module is ensured by an operational amplifier (TL 082). This component provides insulation between the power part and the control part. It protects so as not to exceed the current supplied by the Dspace card, as shown in Figure 11.

Table 9. Parameters of brushless DC motor driver.

Parameter	Value
Rated power	2000 W
Rated voltage	48 V
Continuous current	60 A
Peak current	150 A
Working frequency	16.6 KHz

4. Since the DC bus voltage is 24 V, the input voltage required for the motor driver to operate is 48 V. We have used a step-up DC to DC converter to adapt the voltage level. Its characteristics are presented in Table 10.

Table 10. Parameters of the DC/DC converter.

Parameter	Value
Output power	2016 W
Output current	max. 42 A
Output voltage	48 V
Input voltage	24 V

6.2. Results for No Load Case

Experimental results illustrated the performances of the proposed controller. The phase current waveforms are less ideal than those shown in Figure 6; the BLDC motor suffers from current ripples (see Figures 13–15). Current ripples are considered one of the significant drawbacks of the BLDC motor. Current ripple usually occurs when switching MOSFETs [31].

Referring to the control source, switching the current from one phase to another generates a current ripple phenomenon. The phase currents to be activated and deactivated are not established or cancelled instantaneously in a phase. This is due to the effect of inductance and the rise and fall times of the MOSFETs. The difference between the variation of the phase current establishment slope activated and that of the phase current cancellation deactivated is related to the speed of the motor

Comparing the obtained results shown in Figures 13–15 for the various controllers used in this paper, it is clear that the PSO-PI-ANFIS controller contributed to improving current ripples compared with the rest of the controllers (PI-ANFIS and PI).

The analysis of Figure 16 reveals that the line voltage exhibits a gradual slope owing to the presence of the trapezoidal back-EMF effect. Additionally, the voltage waveform displays narrow pulses. These pulses occur as a consequence of voltage fluctuations resulting from the conduction of the freewheeling diode during the commutation period. The width of these narrow pulses corresponds precisely to the duration of the commutation period, which, in turn, relies on factors such as the electromagnetic time constant and the operating condition of the motor.

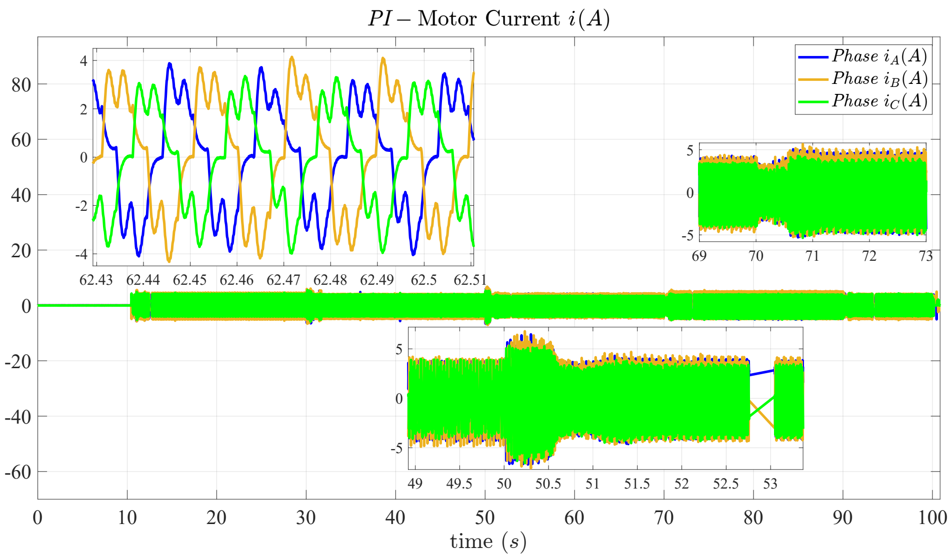

Figure 13. Experimental results of phase currents for speed profile, with the conventional PI controller.

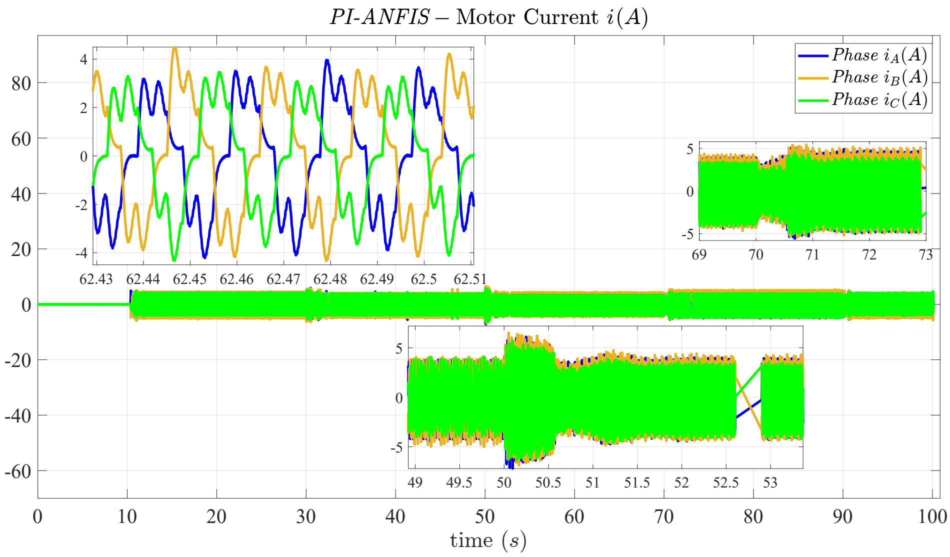

Figure 14. Experimental results of phase currents for speed profile, with the PI-ANFIS controller.

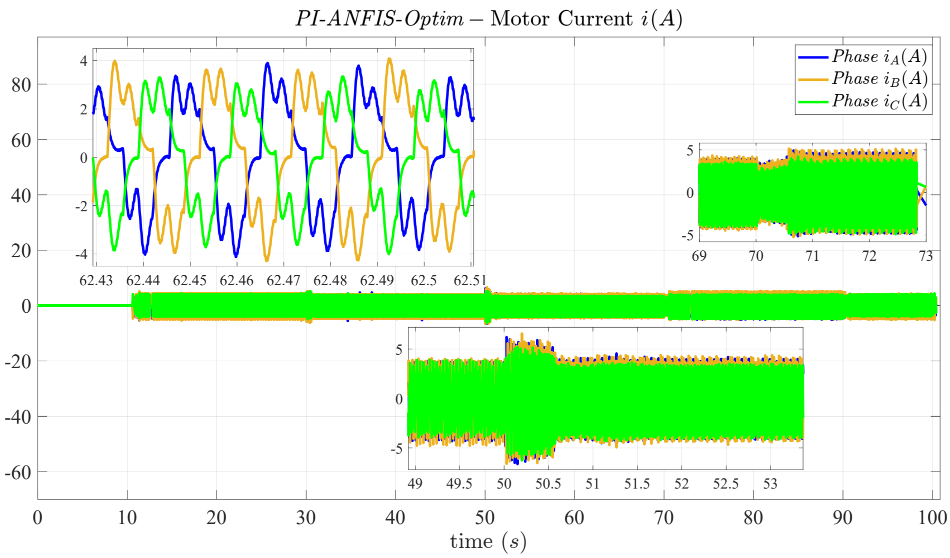

Figure 15. Experimental results of phase currents for speed profile, with the PSO-PI-ANFIS controller.

The experimental results depicted in Figure 17 illustrate the motor speed response for various control modes using the same speed profile. The figure also exhibits the controllers' performance regarding the motor response speed at the reference speed, the amount of overshoot, and the steady-state error. A comparison between the different controllers' results demonstrates that the PSO-PI-ANFIS controller was the most effective in forcing the motor speed to follow the reference speed without overshooting and with no steady-state error. This result indicates the superior control performance of the PSO-PI-ANFIS controller compared to other control units tested in the experiment. The reference speed is the desired speed profile that the motor should follow, while overshoot is an undesirable behavior in which the motor speed exceeds the reference speed before stabilizing. The absence of steady-state error means that the motor's actual speed approaches and remains at the reference speed, indicating the high accuracy and precision of the PSO-PI-ANFIS controller.

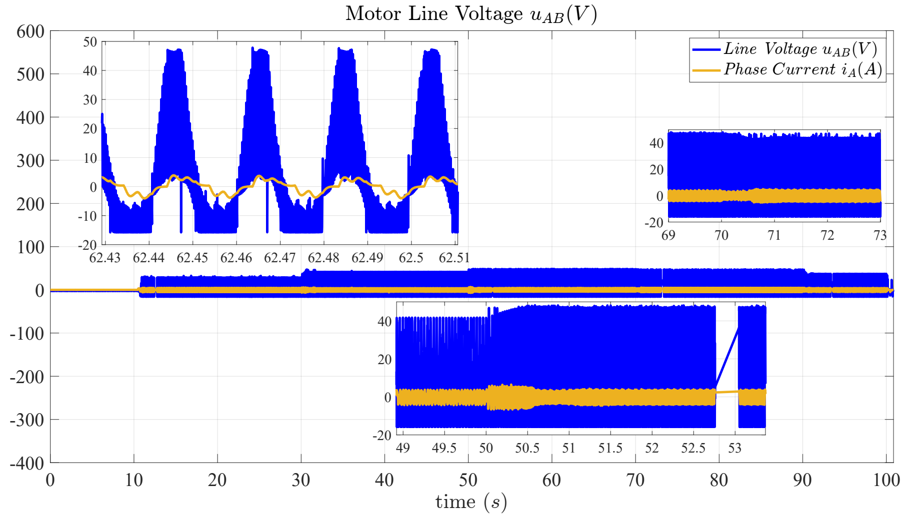

(**a**)

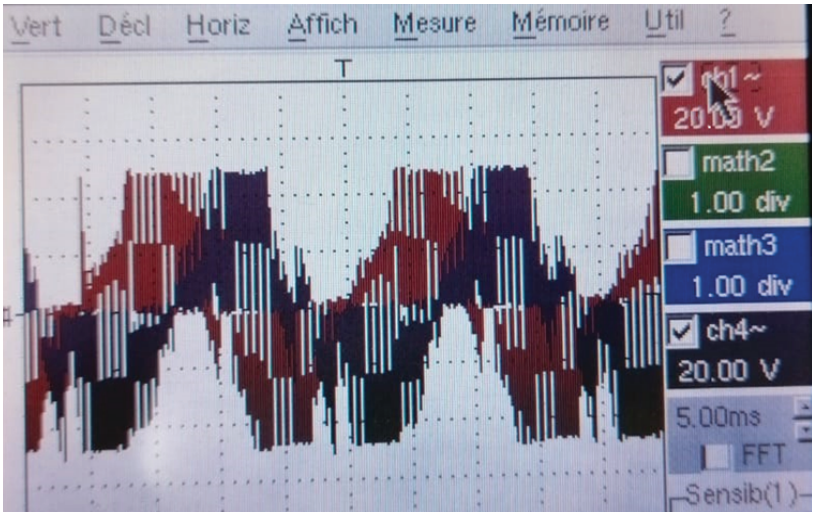

(**b**)

Figure 16. Line voltage of BLDC motor: (**a**) using dSPACE Card. (**b**) using oscilloscope.

The experiment involved measuring the electromagnetic torque values of a BLDC motor that were controlled by different control units while following the same reference speed profile. Figure 18 shows that ripples occurred in the torque waveforms due to changes in the phase currents of the BLDC motor, as seen in Figures 13–15. While the ripples remained acceptable for this type of motor, it was observed that the PSO-PI-ANFIS controller caused minimal ripples compared to the other controllers. This indicates that the PSO-PI-ANFIS controller can achieve smoother and more precise control of the motor's electromagnetic torque.

The experimental results presented in Figure 19 indicate that as the speed of the BLDC motor increases at no load, the fuel cell voltage decreases. This phenomenon can be explained by the fact that an increase in motor speed causes an increase in the load on the fuel cell, which increases the ohmic losses or internal resistance of the fuel cell. Ohmic losses occur due to the resistance of the fuel cell's components, including the electrodes, electrolyte, and interconnects. The increase in ohmic losses leads to a voltage drop across the fuel cell's internal resistance, which causes the fuel cell voltage to decrease.

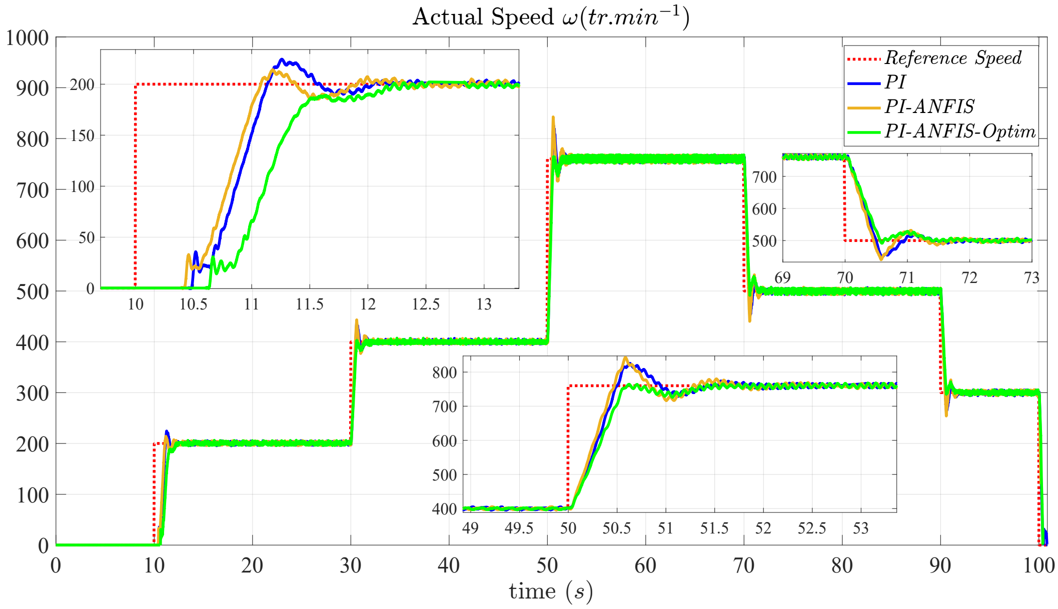

Figure 17. The relationship of rotor speed with time (n).

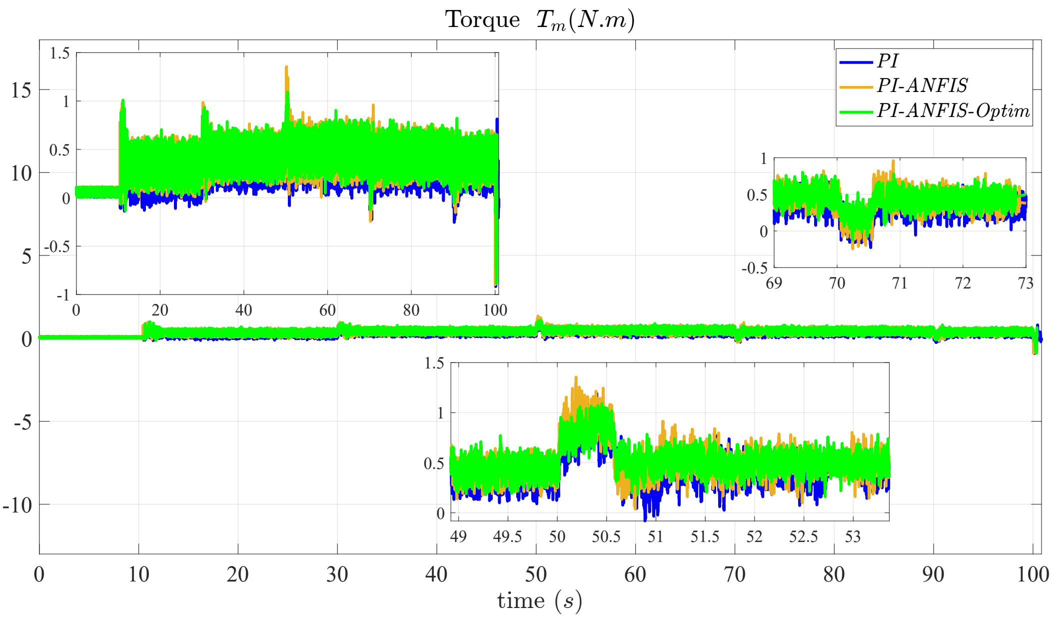

Figure 18. The relationship of electromagnetic torque with time (T_m).

Other factors that can cause a decrease in fuel cell voltage include an increase in load, fuel depletion, and temperature. Conversely, as the speed of the BLDC motor decreases at no load, the load on the fuel cell decreases, reducing the ohmic losses and causing the fuel cell voltage to increase.

The results also indicate that the PSO-PI-ANFIS controller provides better control over the fuel cell voltage compared to the PI-ANFIS controller and the classic PI controller. The PSO-PI-ANFIS controller can optimize the PI gain and parameters of the ANFIS structure using the Particle Swarm Optimization (PSO) algorithm, resulting in improved control performance. The improved control performance is essential in maintaining a stable voltage output from the fuel cell, which is critical for the proper functioning of the system.

The experimental results, as shown in Figure 20, indicate that the fuel cell current changes with respect to the motor speed and load variations. This behavior can be explained by the fact that the fuel cell output power is directly proportional to the load applied to it. Therefore, as the load on the motor increases, the fuel cell has to supply more power, which results in an increase in fuel cell current. Similarly, as the motor speed increases, the fuel cell output power also increases, leading to a rise in fuel cell current. On the other hand, as the load or motor speed decreases, the fuel cell output power decreases, which, in turn, results in a decrease in fuel cell current.

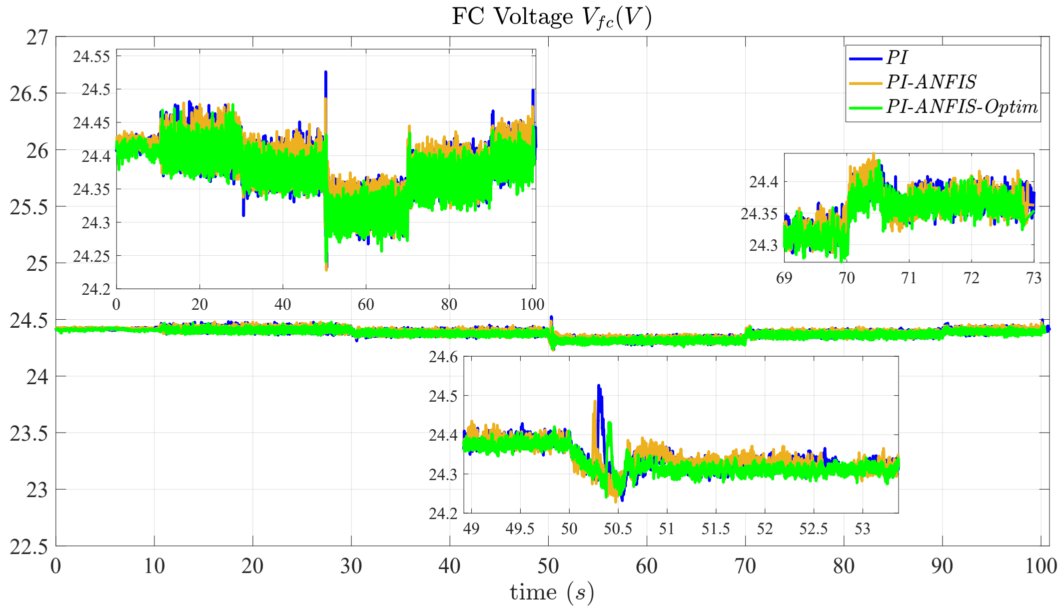

Figure 19. Fuel cell voltage V_{fc}.

Moreover, the internal resistance of the fuel cell also contributes to the change in fuel cell current. As the load on the fuel cell increases, the current flowing through the fuel cell increases, leading to an increase in the voltage drop across the fuel cell's internal resistance. This voltage drop is commonly known as Ohmic losses and can lead to a reduction in fuel cell voltage, causing the fuel cell current to increase to maintain the output power [32]. Similarly, as the motor speed increases, the fuel cell voltage drops due to Ohmic losses, leading to a rise in fuel cell current to maintain the output power.

The results also indicate that the PSO-PI-ANFIS controller provides superior control over the fuel cell current in comparison to the PI-ANFIS and classic PI controllers. Additionally, the DC/DC converter plays a crucial role in regulating the output voltage of the fuel cell to the desired level. The DC/DC converter adjusts the voltage levels of the input and output to maintain a stable voltage and current output. The PSO-PI-ANFIS controller optimizes the gain and parameters of the ANFIS structure using the PSO algorithm to achieve better control performance, resulting in improved current regulation. These findings highlight the importance of utilizing advanced control strategies and appropriate power electronics converters to achieve efficient and stable operation of the fuel cell system.

The experimental results presented in Figure 21 demonstrate the behavior of the DC bus voltage as the motor speed changes under various controllers. The converter used to match the voltage level was successful in maintaining the DC bus voltage around 48 V, despite slight fluctuations observed during the test.

It is noteworthy that the PSO-PI-ANFIS controller showed superior performance in reducing voltage oscillations and sudden changes compared to the other controllers tested. This observation confirms the robustness and effectiveness of the PSO-PI-ANFIS controller in regulating motor speed and maintaining stable voltage levels, even under challenging operating conditions.

These findings suggest that the PSO-PI-ANFIS controller is a promising candidate for applications that require precise and stable motor speed regulation, such as electric vehicles, industrial machinery, and robotics.

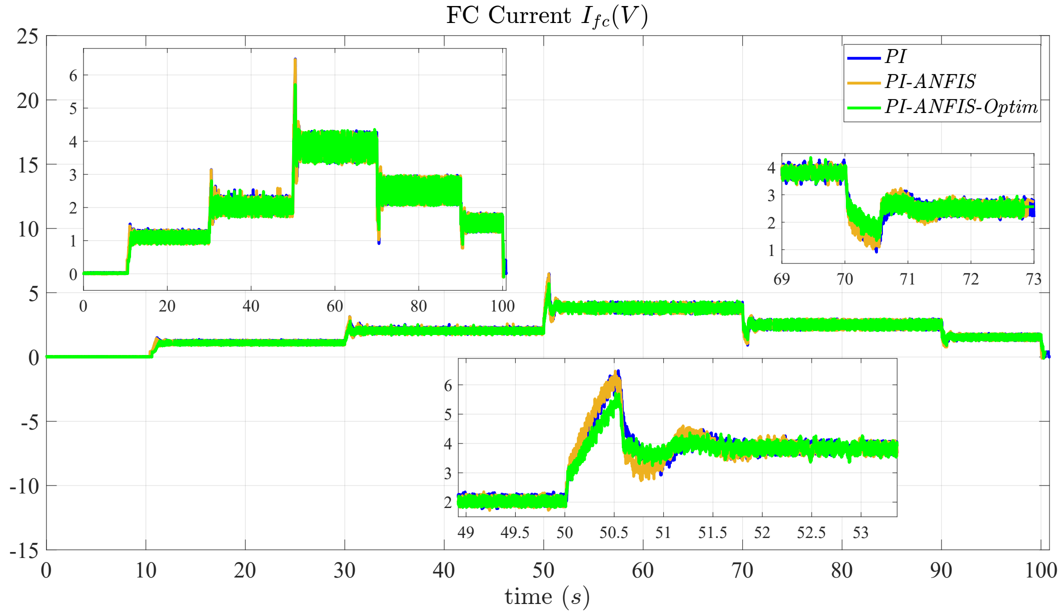

Figure 20. Fuel cell current I_{fc}.

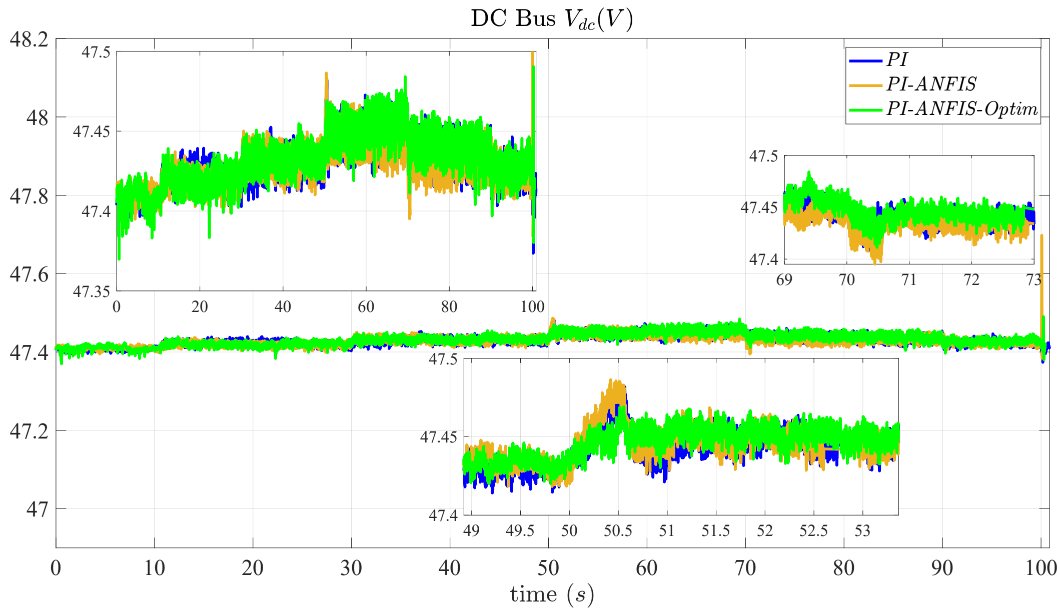

Figure 21. DC bus voltage V_{dc}.

6.3. Results for Varying Load Conditions

The purpose of this section is to assess the performance of different controllers by evaluating their ability to maintain the motor speed at a constant level equal to the reference speed. This is achieved by subjecting the motor to sudden changes in the load, both over time and across different levels. The aim is to measure the effectiveness of each controller in responding to these changes and maintaining stable motor performance under challenging operating conditions.

The electric vehicle motors are constantly subjected to different loading situations caused by various factors, including road curves, grades, and vehicle speed. In order to evaluate and compare different motor control units, a motor can be subjected to a variable load. One method of creating this variable load is by using a combination of a powder brake powered by a power supply and three resistors in series. The resistors can be disconnected and connected in order to change the voltage level and achieve the desired load profile shown in Figure 22. In this section, the speed is set at 500 rpm under many loading conditions. For example, in the first case, the speed is set at 500 revolutions per minute, and the load is changed in stages, starting from zero to an average value, by removing one of the resistors by connecting its two ends with a wire, reaching the maximum (9 nm) by removing the second resistance in a period it lasted 55 s. In the second case, the load is reduced starting from the maximum state (9 nm) through three stations down to the no-load state (0 nm) in 25 s while the speed of the BLDC motor remains constant at 500 rpm.

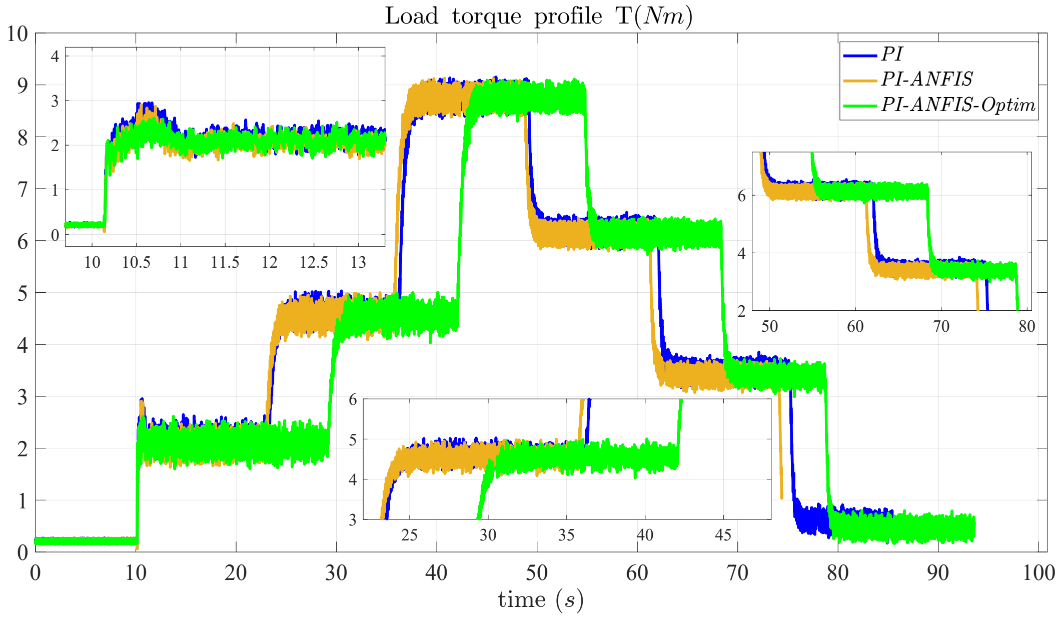

Figure 22. Load torque profile applied by means of powder brake.

The experimental results presented in Figure 23 illustrate the response of the motor speed under various controllers in the presence of a sudden change in load across different values. It is observed that all of the controllers performed well in maintaining the motor speed at a constant level and following the reference speed with high efficiency during the load fluctuation period.

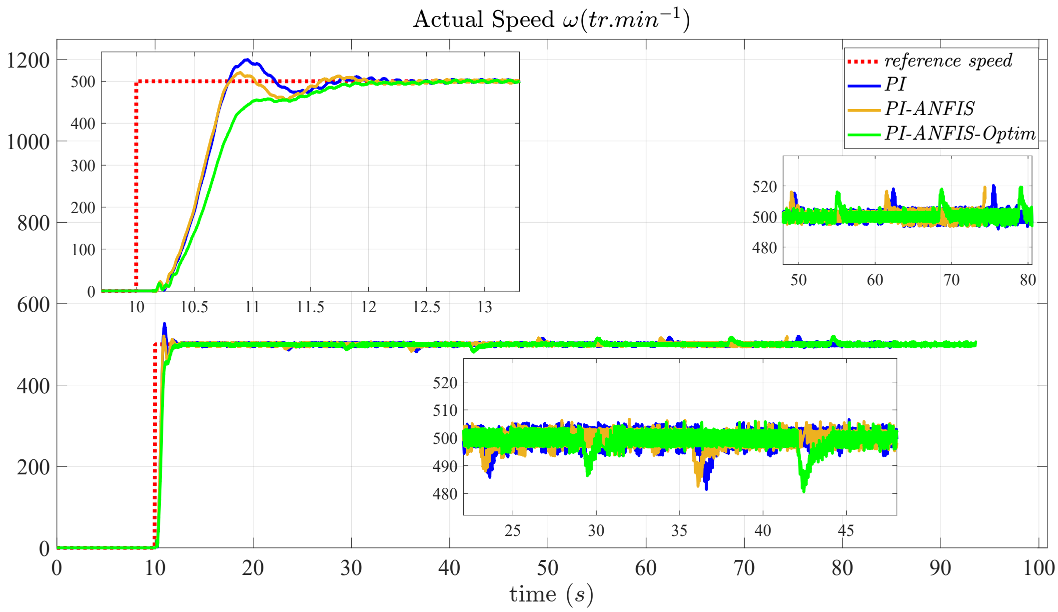

Figure 23. Brushless DC motor speed response under load torque profile applied by means of powder brake.

Comparing the results obtained from different controllers, it can be seen that the PSO-PI-ANFIS controller stands out for its exceptional performance in speed regulation. In addition to maintaining stable motor speed, this controller was also able to reduce motor oscillations, resulting in even better performance under challenging operating conditions.

These results highlight the effectiveness of the PSO-PI-ANFIS controller in controlling motor speed under varying load conditions. This controller can be particularly useful in applications that require precise motor speed regulation and performance optimization, such as electric vehicles, industrial machinery, and robotics.

7. Conclusions and Future Work

The PI algorithm has proven to be a simple and commonly used control method. However, it does not provide perfect control due to the nature of the non-linear systems applied to it. This paper presents for the first time a way to improve the performance of the PI controller by providing gain scheduling by using ANFIS network. Two PI-ANFIS-based architectures have been proposed to control the speed of a brushless DC motor used in electric vehicles that is fed from a pure electric source and an environmentally friendly fuel cell. The hybrid ANFIS method is based on the combination of PSO as the optimization approach and ANFIS. The experimental PI-ANFIS and PSO-PI-ANFIS methods were compared with each other. Comparison results performed on a real platform designed and built in the laboratory show that both approaches presented by PI-ANFIS and PSO-PI-ANFIS force the motor speed to follow its reference precisely. Furthermore, the PSO-PI-ANFIS models with less complex structures are more accurate than the PI-ANFIS models, which is evident from the experimental results obtained above. The main advantages of these methods are their high accuracy and very fast computational speed for prediction and tuning of the parameters of the classical PI controller. Note that the high level of accuracy found in the output results of this controller, especially for the test dataset, indicates that the new proposed PSO-PI-ANFIS approach is reliable. Therefore, from all the previously submitted models, PSO-PI-ANFIS can provide a way to solve the technological problems that we will address after this paper, which are the energy management of the electric vehicle and the reduction in hydrogen consumption.

Author Contributions: Conceptualization, H.E.F. and A.L.; Methodology, A.I., H.E.F. and A.L.; Software, H.H. and S.N.; Validation, A.I., Z.E.I. and A.L.; Formal analysis, A.I.; Investigation, A.I.; Resources, S.N. and A.J.L.; Writing—original draft, A.I.; Supervision, A.I. and H.E.F.; All authors have read and agreed to the published version of the manuscript.

Funding: No external funding was received for this research. The study was conducted without financial support from any external sources or organizations.

Data Availability Statement: The authors are willing to provide access to the data upon request, enabling others to review and utilize the data in accordance with ethical considerations. This promotes transparency and supports the sharing of scientific knowledge within the research community.

Acknowledgments: The authors gratefully acknowledge the support of the Moroccan Ministry of Higher Education (MESRSFC) and the CNRST under grant number PPR/2015/36.

Conflicts of Interest: The authors declare no conflict of interest.

References

1. Azni, M.A.; Md Khalid, R.; Hasran, U.A.; Kamarudin, S.K. Review of the Effects of Fossil Fuels and the Need for a Hydrogen Fuel Cell Policy in Malaysia. *Sustainability* **2023**, *15*, 4033. [CrossRef]
2. Yang, Z.; Jiao, K.; Liu, Z.; Yin, Y.; Du, Q. Investigation of performance heterogeneity of PEMFC stack based on 1+ 1D and flow distribution models. *Energy Convers. Manag.* **2020**, *207*, 112502. [CrossRef]
3. Xu, Y.; Yang, Z.; Jiao, K.; Hao, D.; Du, Q. Development of a comprehensive transient fuel cell-battery hybrid system model and rule-based energy management strategy. *Int. J. Green Energy* **2023**, *20*, 844–858. [CrossRef]
4. Balasankar, A.; Arthiya, S.E.; Ramasundaram, S.; Sumathi, P.; Arokiyaraj, S.; Oh, T.; Aruchamy, K.; Sriram, G.; Kurkuri, M.D. Recent Advances in the Preparation and Performance of Porous Titanium-Based Anode Materials for Sodium-Ion Batteries. *Energies* **2022**, *15*, 9495. [CrossRef]

5. Muthukumar, M.; Rengarajan, N.; Velliyangiri, B.; Omprakas, M.; Rohit, C.; Raja, U.K. The development of fuel cell electric vehicles–A review. *Mater. Today Proc.* **2021**, *45*, 1181–1187. [CrossRef]
6. Shang, Z.; Hossain, M.M.; Wycisk, R.; Pintauro, P.N. Poly (phenylene sulfonic acid)-expanded polytetrafluoroethylene composite membrane for low relative humidity operation in hydrogen fuel cells. *J. Power Sources* **2022**, *535*, 231375. [CrossRef]
7. Mohanraj, D.; Aruldavid, R.; Verma, R.; Sathyasekar, K.; Barnawi, A.B.; Chokkalingam, B.; Mihet-Popa, L. A review of BLDC Motor: State of Art, advanced control techniques, and applications. *IEEE Access* **2022**, *10*, 54833–54869. [CrossRef]
8. Főző, L.; Andoga, R. Advanced Control of an Electric Fuel-Oil Pump for Small Turbojet Engines. *Aerospace* **2022**, *9*, 607. [CrossRef]
9. Nandakumar, M.; Ramalingam, S.; Nallusamy, S.; Srinivasarangan Rangarajan, S. Hall-sensor-based position detection for quick reversal of speed control in a BLDC motor drive system for industrial applications. *Electronics* **2020**, *9*, 1149. [CrossRef]
10. Gamazo-Real, J.C.; Vázquez-Sánchez, E.; Gómez-Gil, J. Position and speed control of brushless DC motors using sensorless techniques and application trends. *Sensors* **2010**, *10*, 6901–6947. [CrossRef]
11. Yigit, T.; Celik, H. Speed controlling of the PEM fuel cell powered BLDC motor with FOPI optimized by MSA. *Int. J. Hydrogen Energy* **2020**, *45*, 35097–35107. [CrossRef]
12. De Lorenzo, G.; Piraino, F.; Longo, F.; Tinè, G.; Boscaino, V.; Panzavecchia, N.; Caccia, M.; Fragiacomo, P. Modelling and Performance Analysis of an Autonomous Marine Vehicle Powered by a Fuel Cell Hybrid Powertrain. *Energies* **2022**, *15*, 6926. [CrossRef]
13. Kim, T.; Yang, J. Control of a brushless DC motor/generator in a fuel cell hybrid electric vehicle. In Proceedings of the 2009 IEEE International Symposium on Industrial Electronics, Seoul, Republic of Korea, 5–8 July 2009; pp. 1973–1977.
14. Tsotoulidis, S.; Mitronikas, E.; Safacas, A. Design of a wavelet multiresolution controller for a fuel cell powered motor drive system. In Proceedings of the XIX International Conference on Electrical Machines—ICEM 2010, Rome, Italy, 6–8 September 2010; pp. 1–6.
15. Feyzi, M.R.; Niapour, S.K.M.; Nejabatkhah, F.; Danyali, S.; Feizi, A. Brushless DC motor drive based on multi-input DC boost converter supplemented by hybrid PV/FC/battery power system. In Proceedings of the 2011 24th Canadian Conference on Electrical and Computer Engineering (CCECE), Niagara Falls, ON, Canada, 8–11 May 2011; pp. 000442–000446.
16. Potnuru, D.; Mary, K.A.; Babu, C.S. Experimental implementation of Flower Pollination Algorithm for speed controller of a BLDC motor. *Ain Shams Eng. J.* **2019**, *10*, 287–295. [CrossRef]
17. Rubaai, A.; Young, P. Hardware/software implementation of fuzzy-neural-network self-learning control methods for brushless DC motor drives. *IEEE Trans. Ind. Appl.* **2015**, *52*, 414–424. [CrossRef]
18. Ibrahim, H.; Hassan, F.; Shomer, A.O. Optimal PID control of a brushless DC motor using PSO and BF techniques. *Ain Shams Eng. J.* **2014**, *5*, 391–398. [CrossRef]
19. Younus, S.M.Y.; Kutbay, U.; Rahebi, J.; Hardalaç, F. Hybrid Gray Wolf Optimization–Proportional Integral Based Speed Controllers for Brush-Less DC Motor. *Energies* **2023**, *16*, 1640. [CrossRef]
20. Wang, C.; Nehrir, M.H.; Shaw, S.R. Dynamic models and model validation for PEM fuel cells using electrical circuits. *IEEE Trans. Energy Conver.* **2005**, *20*, 442–451. [CrossRef]
21. Krein, P.T.; Bentsman, J.; Bass, R.M.; Lesieutre, B.L. On the use of averaging for the analysis of power electronic systems. *IEEE Trans. Power Electron.* **1990**, *5*, 182–190. [CrossRef]
22. Belhaj, F.Z.; El Fadil, H.; El Idrissi, Z.; Intidam, A.; Koundi, M.; Giri, F. New equivalent electrical model of a fuel cell and comparative study of several existing models with experimental data from the pemfc nexa 1200 w. *Micromachines* **2021**, *12*, 1047. [CrossRef]
23. Belhaj, F.Z.; El Fadil, H.; Idrissi, Z.E.; Koundi, M.; Gaouzi, K. Modeling, analysis and experimental validation of the fuel cell association with DC-DC power converters with robust and anti-windup PID controller design. *Electronics* **2020**, *9*, 1889. [CrossRef]
24. Housny, H.; El Fadil, H. Fuzzy PID control tuning design using particle swarm optimization algorithm for a quadrotor. In Proceedings of the 2019 5th International Conference on Optimization and Applications (ICOA), Kenitra, Morocco, 25–26 April 2019; pp. 1–6.
25. Housny, H.; Chater, E.; El Fadhil, H. Multi Closed-lopp Adaptive Neuro-Fuzzy Inference System for Quadrotor Position Control. *Adv. Sci. Technol. Eng. Syst. J.* **2020**, *5*, 526–535. [CrossRef]
26. Jang, J.S. ANFIS: Adaptive-network-based fuzzy inference system. *IEEE Trans. Syst. Man, Cybern.* **1993**, *23*, 665–685. [CrossRef]
27. Kennedy, J.; Eberhart, R.C. A discrete binary version of the particle swarm algorithm. In Proceedings of the 1997 IEEE international Conference on Systems, Man, and Cybernetics, Computational Cybernetics and Simulation, Orlando, FL, USA, 12–15 October 1997; Volume 5, pp. 4104–4108.
28. Nabavi-Pelesaraei, A.; Rafiee, S.; Hosseini-Fashami, F.; Chau, K.w. Artificial neural networks and adaptive neuro-fuzzy inference system in energy modeling of agricultural products. In *Predictive Modelling for Energy Management and Power Systems Engineering*; Elsevier: Amsterdam, The Netherlands, 2021; pp. 299–334.
29. Intidam, A.; El Fadil, H.; El Idrissi, Z.; Lassioui, A.; Rachid, A.; Laafou, A.J. Speed control of a brushless dc motor powered by a pem fuel cell. In Proceedings of the 2021 9th International Renewable and Sustainable Energy Conference (IRSEC), Tetouan, Morocco, 23–27 November 2021; pp. 1–6.
30. Housny, H.; Chater, E.; Fadil, H. Observer-based enhanced ANFIS control for a quadrotor UAV. *Int. Rev. Model. Simul.* **2021**, *14*, 55. [CrossRef]

31. Dahbi, M.; Doubabi, S.; Rachid, A. Current spikes minimization method for three-phase permanent magnet brushless DC motor with real-time implementation. *Energies* **2018**, *11*, 3206. [CrossRef]
32. Intidam, A.; El Fadil, H.; Nady, S.; Gaouzi, K.; El Idrissi, Z.; Koundi, M.; Giri, F. Accounting for current limitation and input saturation in adaptive nonlinear control of fuel cell power system. *Int. J. Emerging Electric Power Systems* **2022**. [CrossRef]